Towards a generalised lattice Boltzmann method for aerodynamic simulations

Juan Antonio Reyes Barraza[a,*], Ralf Deiterding[a]

[a]*School of Engineering, University of Southampton, Boldrewood Campus, SO16 7QF, United Kingdom*

Abstract

The conventional lattice Boltzmann method is restricted to Cartesian grids, making it remarkably expensive for capturing thin boundary layers, and therefore impractical for most relevant problems in aerodynamics. In this paper, a finite difference approach is taken to solve the discrete-velocity Boltzmann equation in generalised curvilinear coordinates to perform fluid flow simulations with non-uniform grids. The present method resolves large gradients in wall vicinity with fewer mesh elements, thereby leading to a reduction in computational effort. Two-dimensional flows at low Reynolds number over circular cylinder and NACA0012 aerofoil are specifically investigated to assess accuracy and performance of the proposed approach.

Keywords: Finite Difference, Non-Uniform Grids, Curvilinear Coordinates

1. Introduction

The lattice Boltzmann method (LBM) is a relatively new development in computational fluid dynamics (CFD), that has emerged as a powerful computational method for the study of fluid dynamic problems. Instead of approximating the Navier-Stokes equations, the approach is based on solving a simplified version of the continuous Boltzmann equation in a specific discrete space. The Navier-Stokes equations in the nearly incompressible flow limit can be derived from the lattice Boltzmann equation (LBE) via the Chapman-Enskog expansion procedure [1]. The simplicity of the LBM algorithm can lead to dramatic reductions in computational time compared to traditional CFD solvers. On uniform grids and applied to unsteady flow simulations, it can easily show performance gains up to two orders of magnitude [2], which has made the approach increasingly popular in recent years for direct numerical simulations of fluid dynamics problems [3].

In the standard LBM, the discretisation of the physical space is coupled with the discretisation of momentum space [4]. The advantage of this is the exact treatment of the advection term, therefore it leads to a scheme without numerical diffusion. The lattice Boltzmann equation typically is solved in a two-step procedure. The first step consists of moving (streaming) the particle distribution function from one lattice point to another, and in the second step the distribution functions are relaxed (collision) locally towards equilibrium. The implementation of the LBM algorithm is relatively straightforward. However, this coupling results in a numerical method that is restricted to Cartesian grids. Therefore, it is difficult to adapt the mesh to complex flows, where higher resolution is needed. This aspect of the standard LBM may limit its application and solving problems with curved geometries and thin boundary layers becomes troublesome.

Yet, the discretisation of the physical space does not necessarily require to be coupled with the moment space [5]. For that reason, it is possible to implement standard numerical techniques on the LBM to use non-uniform and body-fitted grids. In recent years, several efforts have been made to overcome this shortcoming in order to make the LBM a more flexible tool. Some authors have taken different approaches to face the same situation. He et al. [5] have proposed an interpolation scheme for the distribution functions, where the idea is to incorporate an interpolation supplement to determine the distribution functions at the points of interest. The motivation behind this idea is that the particle distribution functions are continuous in space and time. The value of a function at one location can always be approximated by interpolation from the values of their neighbours. This procedure has been used successfully in other works [6, 7]. Another approach consists of interpreting the discrete-velocity Boltzmann equation as an advection equation with a source term. Therefore other authors have applied traditional numerical methods used in CFD, mainly finite differences [8, 9] and finite volume [10, 11, 12], but also there have been some efforts using spectral methods [13, 14]. Consequently, here it is proposed to implement the LBM in generalised curvilinear coordinates, along with standard finite-difference techniques to use non-Cartesian grids.

This paper is organised as follows: In Section 2 the numerical method is presented, including the standard LBM, the transformation to generalised curvilinear coordinates and the numerical schemes used to solve the transformed

*Corresponding author

Email address: j.a.reyes@soton.ac.uk (Juan Antonio Reyes Barraza)

equation. In Section 3 the computational results solely in two dimensions are presented, including the decaying Taylor-Green vortex, the well-known benchmark test-case of the 2D lid-driven cavity flow, the steady and unsteady flow over a 2D circular cylinder and the external flow over the NACA0012 aerofoil in the low Reynolds number regime. The conclusions are given in Section 4.

2. Methodology

In this paper, the implementation is done on the classical D2Q9 LBM-BGK model [15], which describes the evolution of particle distribution functions, $f_\alpha(\mathbf{x}, t)$, in specific discrete directions. Hence, the discrete-velocity Boltzmann equation with single relaxation time and without external forcing may be written as

$$\frac{\partial f_\alpha}{\partial t} + \mathbf{e}_\alpha \cdot \nabla f_\alpha = -\frac{1}{\tau}\left(f_\alpha - f_\alpha^{eq}\right), \quad \alpha = 0, 1..., 8, \quad (1)$$

where τ is the relaxation time, f^{eq} is the equilibrium distribution function, and $\mathbf{e}_\alpha$ is the lattice velocity in the α-direction. In the D2Q9, $\mathbf{e}_\alpha$ can be written as

$$\mathbf{e}_\alpha = \begin{cases} (0,0)c & \alpha = 0 \\ (\cos[(\alpha-1)\pi/4)], & \\ \sin[(\alpha-1)\pi/4])c & \alpha = 1,2,3,4 \\ (\sqrt{2}(\cos[(\alpha-1)\pi/4]), & \\ \sin[(\alpha-1)\pi/4])c & \alpha = 5,6,7,8 \end{cases}, \quad (2)$$

where $c = \Delta x/\Delta t$ is the constant speed for an isothermal model, Δx and Δt are the lattice space and the time step, respectively.

The discretised Maxwell-Boltzmann equilibrium distribution function has been adopted, and it can be written as

$$f_\alpha^{eq} = w_\alpha \rho(x,t)\left[1 + \frac{\mathbf{e}_\alpha \mathbf{u}}{c_s^2} + \frac{(\mathbf{e}_\alpha \mathbf{u})^2}{2c_s^4} - \frac{\mathbf{u}^2}{2c_s^2}\right], \quad (3)$$

where w_α is the weight associated with the discrete velocity $\mathbf{e}_\alpha$, c_s is the speed of sound associated with the model chosen, which is calculated as $c_s = c/\sqrt{3}$, and $\mathbf{u}$ is the macroscopic velocity vector, $\mathbf{u} = (u, v)$. For the D2Q9 model the weight coefficients are $w_0 = 4/9$, $w_1 = w_2 = w_3 = w_4 = 1/9$ and $w_5 = w_6 = w_7 = w_8 = 1/36$.

The macroscopic variables such as mass density and momentum density at $(\mathbf{x}, t)$ can be obtained through the moments of f_α as

$$\rho(\mathbf{x}, t) = \sum f_\alpha(\mathbf{x}, t), \quad \rho\mathbf{u}(\mathbf{x}, t) = \sum f_\alpha(\mathbf{x}, t)\mathbf{e}_\alpha, \quad (4)$$

and the pressure can be directly computed from the isothermal equation of state as

$$p = \rho c_s^2. \quad (5)$$

It can be shown by means of Chapman-Enskog expansion that the presented LBM converges to the weakly compressible Navier-Stokes equations in the low-Mach number limit [16], i.e., to

$$\begin{aligned} &\frac{\partial \rho}{\partial t} + \nabla \cdot (\rho \mathbf{u}) = 0, \\ &\frac{\partial (\rho \mathbf{u})}{\partial t} + \nabla \cdot (\rho \mathbf{u}\mathbf{u}) = -\nabla p + \nu[\nabla^2(\rho\mathbf{u}) + \nabla(\nabla \cdot (\rho\mathbf{u}))]. \end{aligned} \quad (6)$$

Further, the Chapman-Enskog procedure also shows the relation between the kinematic shear viscosity of the fluid ν and the relaxation time as

$$\nu = c_s^2\left(\tau - \frac{\Delta t}{2}\right). \quad (7)$$

Equation (1) can be transformed into a generalised curvilinear coordinate system, in which the independent variables in physical space (x, y) are transformed to a new set of variables in computational space (ξ, η), where

$$\begin{aligned} \xi &= \xi(x, y), \\ \eta &= \eta(x, y). \end{aligned} \quad (8)$$

To perform the transformation from the physical space to the computational space we must apply

$$\begin{aligned} \frac{\partial}{\partial x} &= \frac{\partial}{\partial \xi}\frac{\partial \xi}{\partial x} + \frac{\partial}{\partial \eta}\frac{\partial \eta}{\partial x}, \\ \frac{\partial}{\partial y} &= \frac{\partial}{\partial \xi}\frac{\partial \xi}{\partial y} + \frac{\partial}{\partial \eta}\frac{\partial \eta}{\partial y}. \end{aligned} \quad (9)$$

The physical domain is related to the computational domain by the condition

$$\begin{bmatrix} \xi_x & \xi_y \\ \eta_x & \eta_y \end{bmatrix} = \frac{1}{J}\begin{bmatrix} y_\eta & -x_\eta \\ -y_\xi & x_\xi \end{bmatrix}, \quad (10)$$

where J is the Jacobian of the transformation defined as

$$J = x_\xi y_\eta - x_\eta y_\xi. \quad (11)$$

The convection term in Eq. (1) can be rewritten as

$$\begin{aligned} \mathbf{e}_\alpha \cdot \nabla f_\alpha &= e_{\alpha x}\frac{\partial f_\alpha}{\partial x} + e_{\alpha y}\frac{\partial f_\alpha}{\partial y} \\ &= e_{\alpha x}\left(\frac{\partial f_\alpha}{\partial \xi}\frac{\partial \xi}{\partial x} + \frac{\partial f_\alpha}{\partial \eta}\frac{\partial \eta}{\partial x}\right) + e_{\alpha y}\left(\frac{\partial f_\alpha}{\partial \xi}\frac{\partial \xi}{\partial y} + \frac{\partial f_\alpha}{\partial \eta}\frac{\partial \eta}{\partial y}\right) \\ &= \left(e_{\alpha x}\frac{\partial \xi}{\partial x} + e_{\alpha y}\frac{\partial \xi}{\partial y}\right)\frac{\partial f_\alpha}{\partial \xi} + \left(e_{\alpha x}\frac{\partial \eta}{\partial x} + e_{\alpha y}\frac{\partial \eta}{\partial y}\right)\frac{\partial f_\alpha}{\partial \eta} \\ &= \tilde{e}_{\alpha\xi}\frac{\partial f_\alpha}{\partial \xi} + \tilde{e}_{\alpha\eta}\frac{\partial f_\alpha}{\partial \eta}, \end{aligned} \quad (12)$$

where

$$\tilde{\mathbf{e}}_\alpha = (\tilde{e}_{\alpha\xi}, \tilde{e}_{\alpha\eta}) = (e_{\alpha x}\xi_x + e_{\alpha y}\xi_y, e_{\alpha x}\eta_x + e_{\alpha y}\eta_y). \quad (13)$$

Therefore, the discrete-velocity Boltzmann equation with a single relaxation time in the computational space can be written as

$$\frac{\partial f}{\partial t} + \tilde{e}_{\alpha\xi}\frac{\partial f_\alpha}{\partial \xi} + \tilde{e}_{\alpha\eta}\frac{\partial f_\alpha}{\partial \eta} = -\frac{1}{\tau}\left(f_\alpha - f_\alpha^{eq}\right). \quad (14)$$

Equation (14) is solved in similar manner to the standard LBM. A moving step to advect the particle distribution functions (streaming) and a collision step to relax them toward equilibrium are employed. For simplification, the advection term in Eq. (14) is grouped as

$$A_\alpha = \tilde{e}_{\alpha\xi}\frac{\partial f_\alpha}{\partial \xi} + \tilde{e}_{\alpha\eta}\frac{\partial f_\alpha}{\partial \eta}, \tag{15}$$

which is solved independently of the relaxation process. To solve this term, the spatial derivatives are discretised using finite difference as following:

(a) Central

$$\left.\frac{\partial f_\alpha}{\partial \xi}\right|_{(i,j)} = \frac{f_{\alpha_{(i+1,j)}} - f_{\alpha_{(i-1,j)}}}{2\Delta\xi}. \tag{16}$$

(b) Second order upwind

$$\left.\frac{\partial f_\alpha}{\partial \xi}\right|_{(i,j)} = \frac{3f_{\alpha_{(i,j)}} - 4f_{\alpha_{(i-1,j)}} + f_{\alpha_{(i-2,j)}}}{2\Delta\xi}. \tag{17}$$

(c) Quick

$$\left.\frac{\partial f_\alpha}{\partial \xi}\right|_{(i,j)} = \frac{3f_{\alpha_{(i+1,j)}} + 3f_{\alpha_{(i,j)}} - 7f_{\alpha_{(i-1,j)}} + f_{\alpha_{(i-2,j)}}}{8\Delta\xi}. \tag{18}$$

Here, i and j are the grid indices in the ξ and η directions, respectively. $\frac{\partial f_\alpha}{\partial \eta}$ is also discretised accordingly, and note that the direction of the contravariant velocities $\tilde{e}_{\alpha\xi}$ and $\tilde{e}_{\alpha\eta}$ also has to be considered for the upwind schemes. After the spatial derivatives are discretised, A_α is advanced in the time by using the standard fourth-stage Runge-Kutta scheme as follows:

$$\begin{aligned} f_\alpha^1 &= f_\alpha^t, \\ f_\alpha^2 &= f_\alpha^1 - \frac{\Delta t}{4}A_\alpha^1, \\ f_\alpha^3 &= f_\alpha^1 - \frac{\Delta t}{3}A_\alpha^2, \\ f_\alpha^4 &= f_\alpha^1 - \frac{\Delta t}{2}A_\alpha^3, \\ f_\alpha^* &= f_\alpha^1 - \Delta t A_\alpha^4. \end{aligned} \tag{19}$$

Finally, the method is completed by performing the collision step similarly to the standard LBM as

$$f_\alpha^{t+\Delta t} = f_\alpha^* - \frac{\Delta t}{\tau}\left(f_\alpha^* - f_\alpha^{*eq}\right). \tag{20}$$

Central schemes for convective terms can be unstable when non-linearities are present [17]. Therefore, a fourth order linear damping term is included for the central scheme [14], and it is defined as

$$D_e = -\epsilon_e\left((\Delta\xi)^4\frac{\partial^4 f_\alpha}{\partial \xi^4} + (\Delta\eta)^4\frac{\partial^4 f_\alpha}{\partial \eta^4}\right), \tag{21}$$

where ϵ_e is the dissipation coefficient, and the fourth-order derivatives in Eq. (21) are approximated by central difference as

$$\begin{aligned} (\Delta\xi)^4\left.\frac{\partial^4 f_\alpha}{\partial \xi^4}\right|_{(i,j)} =& f_{\alpha_{(i-2,j)}} - 4f_{\alpha_{(i-1,j)}} + 6f_{\alpha_{(i,j)}} - \\ & 4f_{\alpha_{(i+1,j)}} + f_{\alpha_{(i+2,j)}}, \\ (\Delta\eta)^4\left.\frac{\partial^4 f_\alpha}{\partial \eta^4}\right|_{(i,j)} =& f_{\alpha_{(i,j-2)}} - 4f_{\alpha_{(i,j-1)}} + 6f_{\alpha_{(i,j)}} - \\ & 4f_{\alpha_{(i,j+1)}} + f_{\alpha_{(i,j+2)}}. \end{aligned} \tag{22}$$

The dissipation term is added explicitly to Eq. (15) in the same manner as by Hoffmann et al. [17], $f_\alpha^* = f_\alpha^* + D_e$.

The objective of the linear damping term, also known as artificial dissipation, is to stabilise the solution for the central space discretisation against spurious oscillations that may be generated by the boundary conditions and non-linearities in the flow field. The dissipation coefficient is constant in the domain, and it does not change throughout the time iterations. Each linear damping term is of an even order derivative, with a truncation error lower than the truncation error of the selected space discretisation, otherwise, it would affect the formal order of the scheme. For instance, a fourth-order space discretisation requires at least a sixth-order linear damping [18].

Modified wavenumber analysis shows that upwind schemes introduce numerical dissipation into the solution, and hence they can damp any spurious oscillations naturally [19]. However, contrary to central difference schemes, which do not have any dissipation error arising from the spatial discretisation, choosing an optimal amount of numerical dissipation in an upwind discretisation that stabilises the numerical solution [20], and at the same time avoids an excessively smeared out approximation, is intrinsically difficult.

3. Computational Results

Four test cases are carried out to validate and to show that the implemented methodology is accurate and reliable. These are the decaying Taylor-Green vortex, the 2D lid-driven cavity flow, steady and unsteady flows over a 2D circular cylinder and the NACA0012 aerofoil in the low Reynolds number regime at different conditions. The results are compared with available numerical and experimental data. Also, the present method is compared with our in-house Cartesian LBM solver, AMROC-LBM [2], with adaptive mesh refinement to demonstrate the superior capabilities of the non-Cartesian approach to resolve the flow in the vicinity of the wall for curved geometries. Only for the first test case, different schemes are used to discretise the spatial derivatives, and it is for comparison purposes. For the rest of the numerical simulations, only the central scheme is used. All simulations have a characteristic velocity equal to 0.1 and a dissipation coefficient ϵ_e equal to 0.001, unless otherwise specified.

3.1. Taylor-Green Vortex Flow

The Taylor-Green vortex decay has been widely used for the verification of incompressible flow solvers, since its solution has an analytical expression. The Taylor-Green flow is periodic in a domain of size $L_x \times L_y$ and its structure is maintained while decaying exponentially [21]. This benchmark test is done to compare the accuracy of the different spatial schemes and to verify the capacity of the present methodology to use non-uniform grids. The exact solution of this unsteady problem in two dimensions is given by

$$\begin{aligned} u(\mathbf{x},t) =& - u_o\sqrt{\left(\frac{k_y}{k_x}\right)}\cos(k_x x)\sin(k_y y)e^{\frac{-t}{t_d}}, \\ v(\mathbf{x},t) =& u_o\sqrt{\left(\frac{k_x}{k_y}\right)}\sin(k_x x)\cos(k_y y)e^{\frac{-t}{t_d}}, \\ p(\mathbf{x},t) =& p_0 - \rho\frac{u_o^2}{4}\left[\frac{k_y}{k_x}\cos(2k_x x) + \frac{k_x}{k_y}\cos(2k_y y)e^{(\frac{-2t}{t_d})}\right]. \end{aligned} \tag{23}$$

In this case, u_o is the initial velocity, ν is the kinematic viscosity of the fluid, $k_x = 2\pi/L_x$ and $k_y = 2\pi/L_y$ are the wavenumbers in x- and y-direction. t_d is the vortex decay time, and it is defined as

$$t_d = \frac{1}{\nu(k_x^2 + k_y^2)}. \tag{24}$$

The initial conditions for the velocity and pressure fields are obtained by setting $t = 0$.

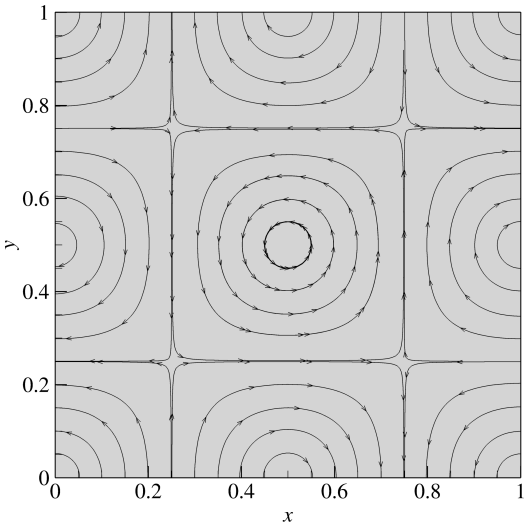

Figure 1: Taylor-Green vortex structure shown by streamlines.

A clustering function has been selected to stretch the mesh in both directions, x and y. The grid can be stretched by applying

$$x = H\frac{(2\alpha+\beta)[(\beta+1)/(\beta-1)]^{(\xi-\alpha)/(1-\alpha)} + 2\alpha - \beta}{(2\alpha+1)\left(1+[(\beta+1)/(\beta-1)]^{(\xi-\alpha)/(1-\alpha)}\right)}, \tag{25}$$

$$y = H\frac{(2\alpha+\beta)[(\beta+1)/(\beta-1)]^{(\eta-\alpha)/(1-\alpha)} + 2\alpha - \beta}{(2\alpha+1)\left(1+[(\beta+1)/(\beta-1)]^{(\eta-\alpha)/(1-\alpha)}\right)}, \tag{26}$$

where β is the clustering parameter, α defines where the clustering takes place, and H is the length. If $\alpha = 0.5$, the clustering is distributed equally, and if $\alpha = 0$ the clustering takes place at H. Here, all the computations are performed with $\alpha = 0.5$ and $\beta = 1.2$.

Figure 2 shows the non-uniform grid of 65×65 size, that can be obtained by applying the clustering functions previously described, and the initial flow field shown by streamlines can be seen in Figure 1. The present methodology is compared with the analytical solution at a dimensionless time of 0.1, $t^* = tu_o/L_{ref}$. For this first test-case, a computational grid of 33×33 nodes was used, the characteristic velocity u_o is 0.01, and a Reynolds number of 100 was selected.

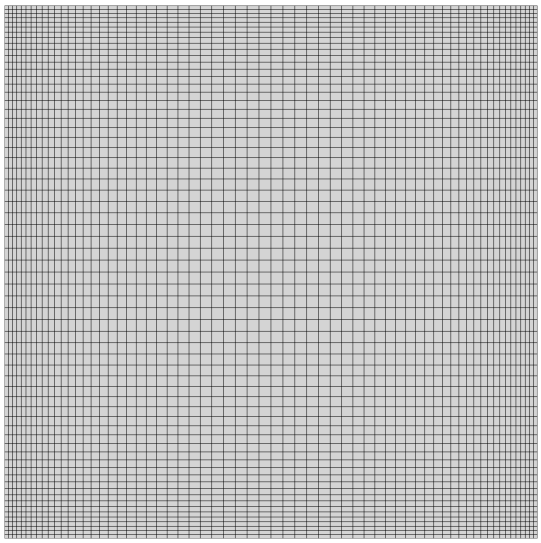

Figure 2: Non-uniform grid used for the Taylor-Green vortex and the 2D lid-driven cavity.

Figure 3 shows the velocity components (u, v) normalised by u_o at the mid-width and mid-height of the domain. The numerical solutions of the central, QUICK and second order upwind (SOU) for the advection term are compared with the analytical solution in Figure 3. SOU shows severe dissipation levels. The dissipation shown by the QUICK scheme is not as severe as the SOU scheme, but it is more than the central scheme. This behaviour can be expected as it is known that upwind schemes are more dissipative than central schemes. Note that it is not necessary to apply the linear damping to the QUICK and SOU space discretisations. The fourth-order linear damping previously

described is used only on the central scheme, and it can be observed that the effect on the numerical solution is negligible, since the linear damping is of a higher order than the numerical scheme.

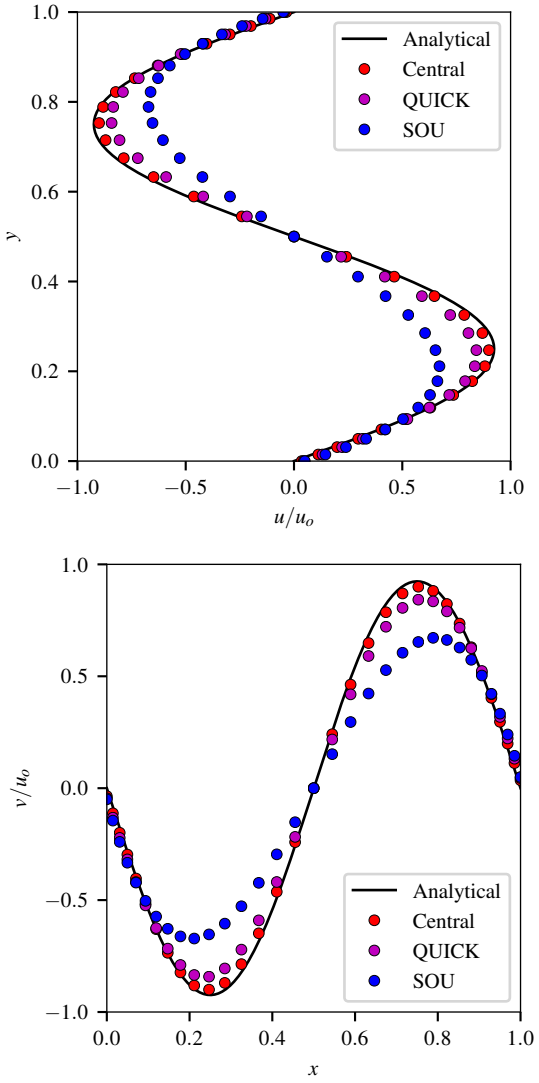

Figure 3: Velocity profiles: Normalised u-velocity along the vertical centreline (top) and normalised v-velocity along the horizontal centreline (bottom).

Several simulations are carried out on uniform grids with the central space discretisation in order to assess numerically the order of accuracy of the scheme. The u-velocity profile along the vertical centreline is compared with the analytical solution as well as with a high-resolution numerical solution for three different times. Two characteristic velocities ($u_0 = 0.01$ and $u_0 = 0.005$) are used for the analysis, and the L_2-norm is used to assess the error. The numerical reference solution has a resolution of 321×321, and it was obtained for the two different characteristic velocities and the three dimensionless times.

The results of the order of accuracy analysis are shown in Tables 1 and 2 for two different Mach numbers $M_a = u_o/c_s$. They contain the grid size used, $\tilde{\tau}$ defined as $\tilde{\tau} = \tau/\Delta t$ and the L_2-norm for three different dimensionless times. It can be noticed that the order of accuracy estimated is slightly higher when the numerical solution is used to assess the error. Even so, the results confirm that the central scheme implemented is a second-order accurate numerical method, and that the fourth-order linear damping does not affect the formal order of accuracy of the scheme.

Table 1: L_2-norm error of u-velocity for Re = 100, $u_o = 0.01$, and $Ma \approx 0.017$.

		Dimensionless time t*		
Grid	$\tilde{\tau}$	0.1	0.2	0.3
21	0.56	0.1967	0.2401	0.2697
41	0.62	0.0522	0.0630	0.0686
81	0.74	0.0174	0.0218	0.0238
Order of accuracy		∼1.75	∼1.73	∼1.75
		Relative to the analytical solution.		
		Dimensionless time t*		
Grid	$\tilde{\tau}$	0.1	0.2	0.3
21	0.56	0.1855	0.2301	0.2616
41	0.62	0.0446	0.0547	0.0600
81	0.74	0.0125	0.0161	0.0178
Order of accuracy		∼1.94	∼1.92	∼1.94
		Relative to the numerical solution.		

Table 2: L_2-norm error of u-velocity for Re = 100, $u_o = 0.005$, and $Ma \approx 0.009$.

		Dimensionless time t*		
Grid	$\tilde{\tau}$	0.1	0.2	0.3
21	0.53	0.2593	0.3549	0.4224
41	0.56	0.0568	0.0696	0.0763
81	0.62	0.0176	0.0226	0.0252
Order of accuracy		∼1.94	∼1.99	∼2.03
		Relative to the analytical solution.		
		Dimensionless time t*		
Grid	$\tilde{\tau}$	0.1	0.2	0.3
21	0.53	0.2505	0.3486	0.4184
41	0.56	0.0494	0.0616	0.0683
81	0.62	0.0127	0.0169	0.0192
Order of accuracy		∼2.15	∼2.18	∼2.22
		Relative to the numerical solution.		

3.2. 2D Lid-Driven Cavity

The 2D lid-driven cavity is a classical benchmark test, thanks to its simple geometry yet complex flow physics [22]. It consists of the movement of the top-lid at a constant velocity u_o and three stationary walls ($u = v = 0$). The geometry normally is a square, but this may be different. This test case is validated with a non-uniform grid, where the same clustering function employed for the Taylor-Green vortex is used to distribute the grid elements increasing the resolution in the corners.

For moderate and high Reynolds number, the 2D lid-driven cavity produces central cores where the vorticity

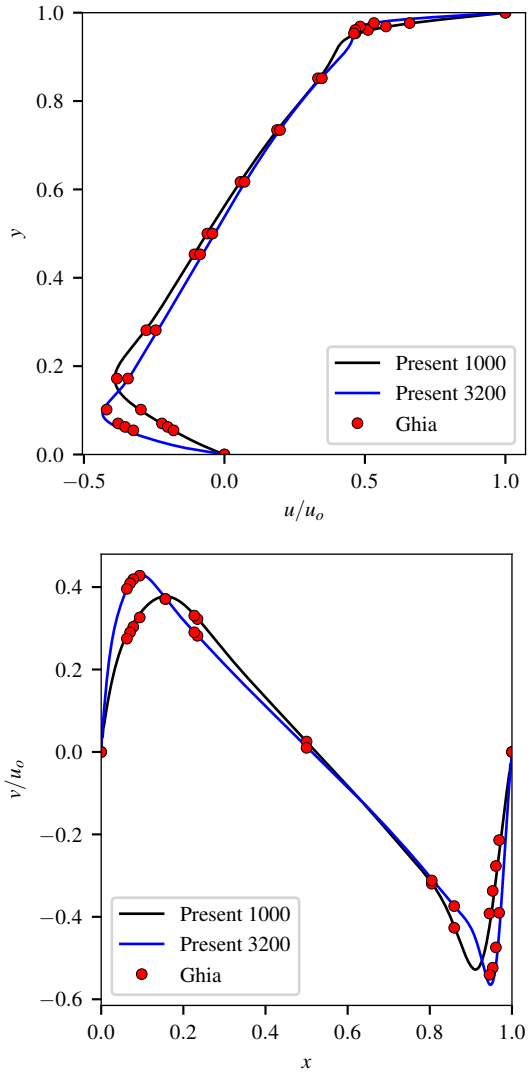

Figure 4: Velocity profiles: Normalised u-velocity along the vertical centreline (top) and normalised v-velocity along the horizontal centreline (bottom) for Re = 1000 and Re = 3200.

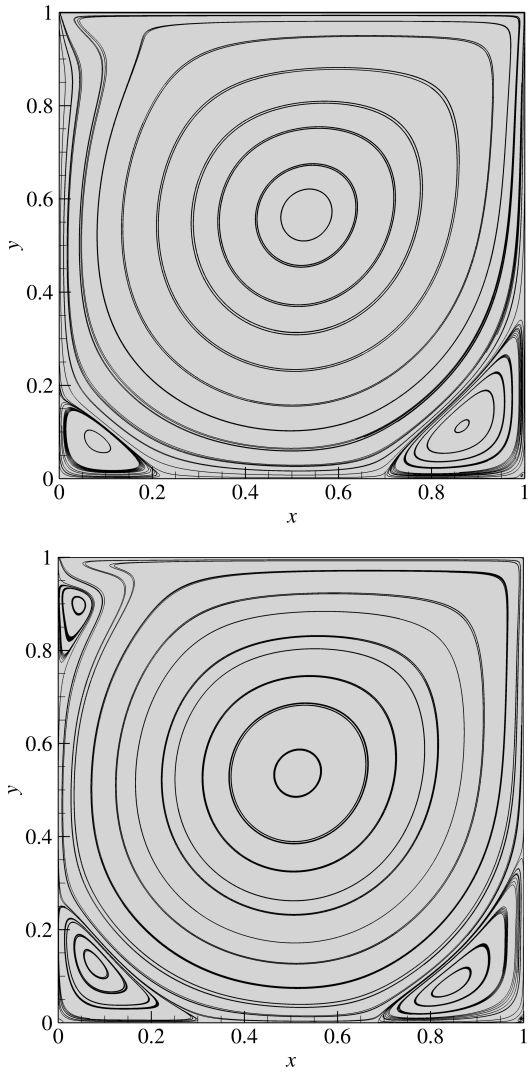

Figure 5: Flow field shown by streamlines for Re = 1000 (top) and Re = 3200 (bottom).

can be considered constant [23]. The viscous effects are seen close to the walls where they are confined in shear layers. Besides, in the inferior corners, small counter-rotating vortices are produced, which can be difficult to capture. Therefore, it is desirable to use non-uniform grids and refine the mesh near the corners and walls. The simulations are carried out on a grid resolution of 257×257 for the Re = 1000 and 513×513 for Re = 3200.

There is no exact solution for the 2D cavity flow. Because of this we need to compare our results with a comprehensive study, such as the one done by Ghia et al. [22]. The u-velocity profile along the vertical centreline, the v-velocity profile along the horizontal centreline and the streamlines for the two different Reynolds numbers are shown in Figures 4 and 5. Our results have excellent agreement with the reference [22], and the streamlines show a correct flow behaviour in the entire domain. It is known that the corners are singularity points, and our results do not exhibit any issues in these regions, demonstrating the capability of the current methodology and the proper application of the stretching function on the grid.

3.3. 2D Circular Cylinder

The wall-boundary treatment of the previous test cases is relatively straightforward since there are no curved walls. Therefore, the 2D circular cylinder is used to demonstrate the capacity of the present method to perform steady and unsteady simulations with curved surfaces. Furthermore, proper stretching functions have been implemented to increase the resolution in the proximity of the wall and the wake region. Our results have been compared with the literature available, and the outcomes of the present method are consistent with other results, supporting the proposed scheme. Additionally, the present method is compared to our own Cartesian LBM solver AMROC-LBM [2].

Unlike most LBM solvers, in AMROC-LBM (Adaptive Mesh Refinement in Object-oriented C++) it is pos-

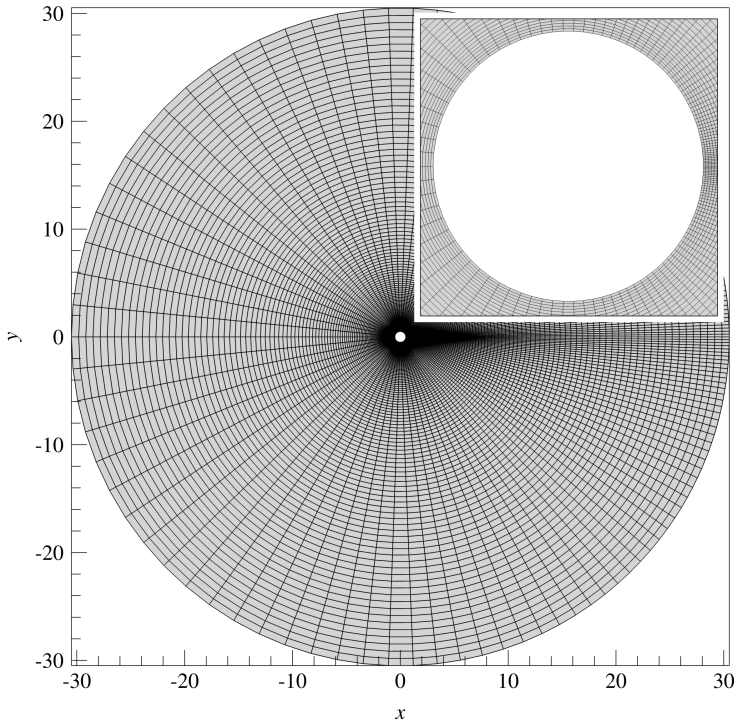

Figure 6: O-Grid for the 2D Cylinder Mesh. Overlaid on the upper right is a close-up of the body-confirming mesh around the cylinder.

sible to have non-uniform Cartesian grids and therefore increase the resolution in areas of interest. It is relatively easy to apply isotropic mesh adaptation to the standard LBM, and thereby resolving laminar boundary layers [16]. Nonetheless, this approach can become remarkably expensive for capturing boundary layers of turbulent flows, and therefore it is impractical for most relevant problems in aerodynamics. Instead of using isotropic refinement of individual cells, AMROC-LBM uses block-structured mesh refinement [24], which is more computationally efficient. The mesh adaptation algorithm of AMROC-LBM is mathematically equivalent to the algorithm by Chen et al. [25], and it has been verified and validated previously [26]. AMROC-LBM contains the classical LBM models in two and three dimensions such as D2Q9, D3Q19, and D3Q27. In this work, AMROC is using the D2Q9 model with single relaxation time. Note that in the block-structured mesh adaptation approach, the computational update is accomplished by calling a single-block routine successively on the sequence of block-structured sub-grids. In AMROC-LBM, this single-block routine is literally identical to a conventional LBM implementation tailored for high performance on a single uniform mesh, and when the software is running in unigrid mode, i.e. without mesh adaptation, the computational performance of a quasi-optimal unigrid LBM implementation is fully retained.

For the following, an O-grid with an outer diameter 30 times larger than the inner diameter was used (cf. Fig. 6). A uniform velocity with zero pressure gradient is applied to the inlet, a no-slip wall boundary condition is imposed at the cylinder surface, a classical outlet with constant pressure is enforced, and periodic boundaries are being used for the wake region. Imposing boundary conditions for the LBM is quite different than with traditional CFD solvers, since it is necessary to determine the distribution functions, and not only the macroscopic variables. Therefore, the ideas from Guo et al. [27] were extended to non-Cartesian meshes to impose the boundary conditions.

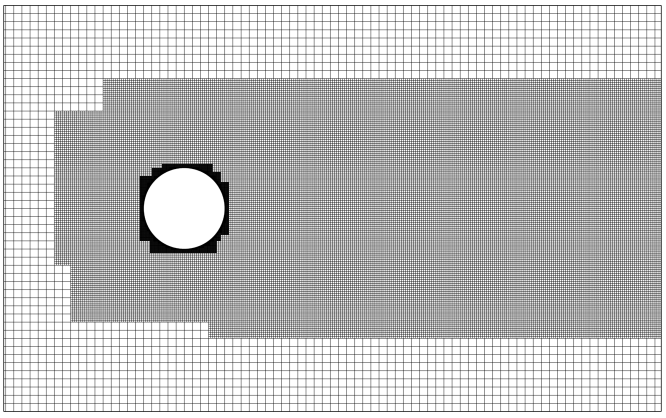

Figure 7: Snapshot of AMROC-LBM mesh of the steady flow passing the circular cylinder at Re = 40.

The following function is used for the stretching in the

Table 3: Effects of the Reynolds number on steady flow over the circular cylinder.

Re	Author(s)	C_d	$C_p(180)$	$C_p(0)$	$2L/D$	θ_s
20	Tritton [28]	2.10	-	-	-	-
	Henderson [29]	2.06	-	-0.60	-	-
	Dennis and Chang [30]	2.05	1.27	-0.58	1.88	43.70
	He et al. [6]	2.15	1.28	-0.58	1.84	42.96
	Patil and Lakshmisha [12]	1.95	1.21	-0.54	1.88	42.81
	AMROC-LBM	1.99	1.28	-0.59	1.84	43.66
	Present	2.02	1.31	-0.55	1.85	43.87
40	Tritton [28]	1.59	-	-	-	-
	Henderson [29]	1.55	-	-0.53	-	-
	Dennis and Chang [30]	1.52	1.14	-0.50	4.69	53.80
	He et al. [6]	1.49	1.11	-0.48	4.49	52.84
	Patil and Lakshmisha [12]	1.55	1.15	-0.49	4.28	52.74
	AMROC-LBM	1.45	1.21	-0.50	4.47	53.37
	Present	1.51	1.19	-0.46	4.60	53.98

wall normal direction

$$y_n = \delta \frac{(1-\beta)\left(\frac{\beta+1}{\beta-1}\right)^{1-\xi} + (\beta+1)}{\left(\frac{\beta+1}{\beta-1}\right)^{1-\xi} + 1} + r, \quad 0 \leq \xi \leq 1, \quad (27)$$

where δ is the radial distance between the body and the outer boundary, β is the clustering parameter which has been set to 1.007 for these simulations and r is the radius of the cylinder. The grid clustering function shown in Eq. (26) was used to increase the resolution behind the cylinder. The clustering parameter used for the wake is 1.045.

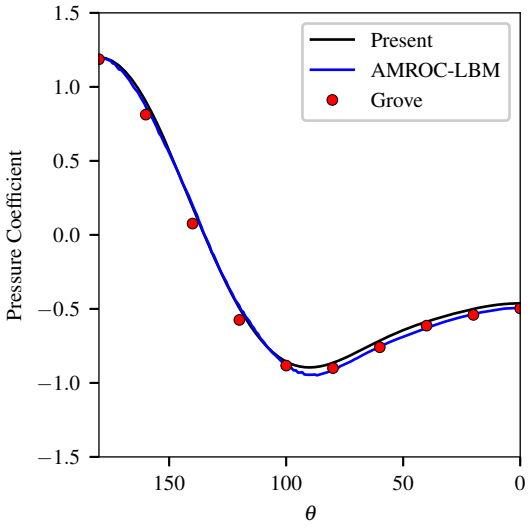

Figure 8: Pressure coefficient over the surface of the circular cylinder at Re = 40.

Two Reynolds numbers were selected for the steady-state simulations, 20 and 40. At these flow conditions, stationary recirculation regions appear for both cases behind the cylinder, and these increase in length as the Reynolds number increases, as it can be seen in Figure 10. The literature shows that the recirculating regions appear around $5 < \mathrm{Re} < 47$. For Reynolds numbers below 5 the flow will remain attached; above the critical Reynolds number, which is about 47, the solution will be unsteady.

The comparison of the steady-state results is shown in Table 3. The references used are quite vast and they include the numerical solutions of the Navier-Stokes equations from Henderson [29], Dennis and Chang [30], experimental data from Tritton [28], LBM with the interpolation supplement from He and Doolen [6], and a finite volume TDV formulation of the LBM on unstructured meshes from Patil and Lakshmisha [12]. The variables presented are the drag coefficient C_d, the pressure coefficient at the stagnation point $C_p(180)$ and at the rear-point $C_p(0)$, the length of the wake normalised by the diameter $2L/D$, and the separation angle θ_s. Table 3 shows that our results exhibit good agreement with diverse references, and Figure 8 shows the pressure coefficient distribution over the cylinder for the present methodology, AMROC-LBM and the experimental data from Grove et al. [31] for Reynolds number 40.

In order to highlight the accuracy of the present scheme on curved geometries, a convergence error analysis was conducted for this test-case. The computations are carried out on different grids resolutions, namely, 129×129, 193×193, 257×257, and 513×513, at Reynolds number 40. The absolute error of the drag coefficient is used for the analysis, and the finest grid value is considered as the reference solution. Figure 9 shows the slope corresponding to second-order-accurate convergence versus the errors produced by the present scheme. It can be observed that the error obtained by the current methodology decreases with second order, thereby the order of the scheme remains unaltered for curved geometries.

For the unsteady test case, two laminar flows at 100

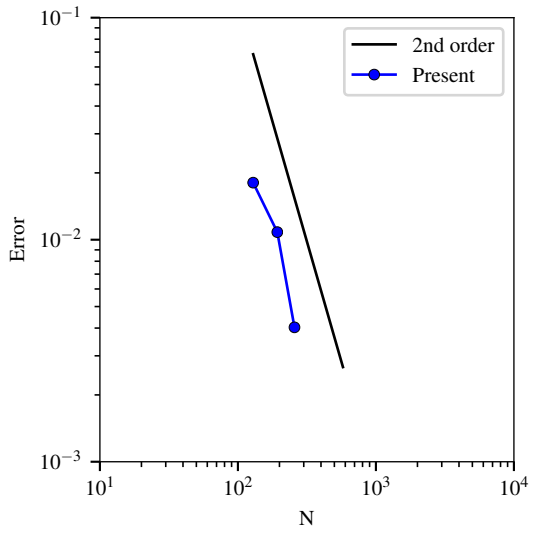

Figure 9: Absolute error based on C_d against the number of grid elements (N) in each direction for the 2D circular cylinder at Re = 40.

and 200 Reynolds number were selected. These simulations demonstrate the capacity of the presented method to simulate time-dependent flows around geometries with curved wall-boundaries. At these flow conditions, the recirculation regions behind the cylinders become unstable, and time-periodic vortex-shedding solutions appear. The dimensionless number used to characterise this phenomenon is the Strouhal number that is defined as $\mathrm{St} = f_q D/u_o$, where f_q is the shedding frequency. The Strouhal number can also be written as $\mathrm{St} = D/u_o T_p$, where T_p is the period of the lift coefficient signal.

Table 4: Effects of the Reynolds number on unsteady flow over the circular cylinder.

Re	Author(s)	St	$\overline{C_d}$	C_l'
100	Chiu et al. [32]	0.167	1.35	0.30
	AMROC-LBM	0.165	1.25	0.34
	Present	0.165	1.37	0.35
200	Chiu et al. [32]	0.198	1.37	0.71
	AMROC-LBM	0.196	1.26	0.71
	Present	0.196	1.37	0.73

Table 4 compares the present time-depended solutions with the reference selected and as well as with the results obtained using AMROC-LBM. The Navier-Stokes solutions from Chiu et al. [32] are used as a reference. The variables compared are the Strouhal number St, the average drag coefficient $\overline{C_d}$ and the lift coefficient amplitude C_l'. The results produced by the LBM in generalised curvilinear coordinates have an excellent agreement with the reference for all the variables compared. The results obtained by AMROC-LBM also have a good agreement for the variables compared.

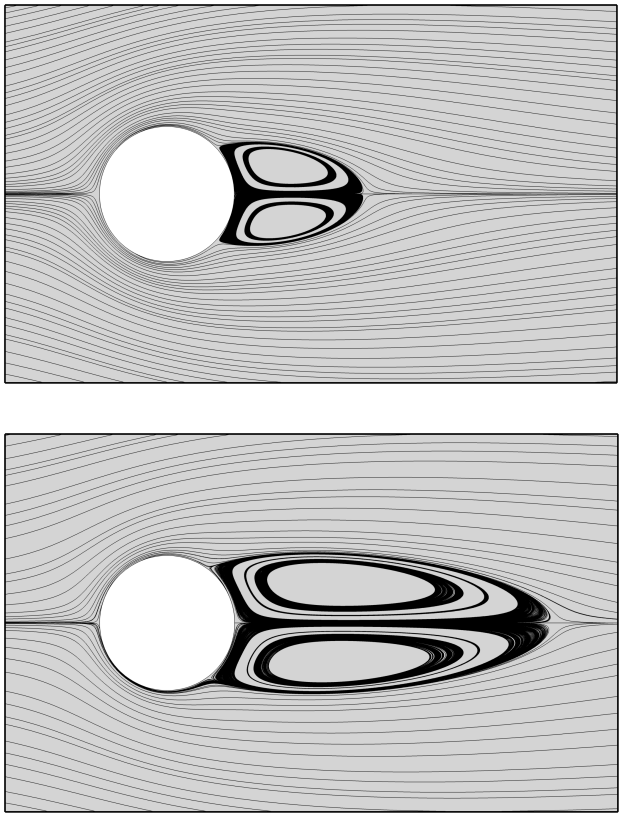

Figure 10: Flow field for steady flow over the 2D circular cylinder shown by streamlines using the implemented methodology. Top: Re = 20. Bottom: Re = 40.

A series of simulations with different resolutions are performed using the present methodology and AMROC-LBM. The Mach number is set to $\sqrt{3}/10$ and both solvers are running up to the same dimensionless time, which is sufficiently large to stabilise the solution in the steady-state cases and yield a reliably periodic result in the time-dependent cases. The clustering parameters remain unchanged for the finite-difference LBM solver, and the grid always has the same number of points on the wall-surface and in the wall-normal direction, i.e., 129×129, 257×257, and 385×385. The simulations carried out using the Cartesian LBM with adaptive mesh refinement (cf. Fig. 7) are performed on a domain size of $[-14D \times 40D] \times [-14D \times 14D]$ using a base mesh of 540×280 cells for the steady-state simulations and 1080×560 for the unsteady flow, with the axis origin at $(x, y) = (0, 0)$. The adaptive mesh refinement algorithm is using up to 3 additional levels, and each level is uniformly refined with a factor of 4. Also, simulations are run with a fixed refinement patch of $[-1.5D \times 5D] \times [-1.75D \times 1.75D]$ for the wake and up to 2 additional levels for the wall refinement. Simulations with uniform grids are also included.

Table 5 compares the CPU time, the number of mesh elements, the C_d for the the steady-state cases and the C_l' for the unsteady-state for the cases run. This table

Table 5: Comparison in terms of number of mesh elements and CPU time between the present implementation, AMROC-LBM, AMROC-LBM* with a fixed refined patch, and AMROC-LBM (uni.) with uniform mesh. CPU time is given in hours.

Re = 20			
Method	Mesh	CPU time	C_d
AMROC-LBM (uni.)	9,676,800	236.78	1.58
AMROC-LBM (uni.)	2,419,200	30.01	1.30
AMROC-LBM*	263,920	16.51	1.99
AMROC-LBM	272,576	16.95	1.99
Present	65,536	6.16	2.02
Present	16,384	0.81	2.03
Re = 40			
Method	Mesh	CPU time	C_d
AMROC-LBM (uni.)	15,120,000	479.78	1.16
AMROC-LBM (uni.)	9,676,800	240.58	1.12
AMROC-LBM*	263,920	17.43	1.44
AMROC-LBM	294,384	18.73	1.45
Present	65,536	5.95	1.51
Present	16,384	0.72	1.53
Re = 100			
Method	Mesh	CPU time	C_l'
AMROC-LBM*	905,440	71.32	0.34
AMROC-LBM	876,336	77.20	0.34
Present	147,456	20.75	0.35
Present	65,536	5.98	0.36
Re = 200			
Method	Mesh	CPU time	C_l'
AMROC-LBM*	905,440	70.71	0.71
AMROC-LBM	972,880	78.52	0.71
Present	147,456	20.45	0.73
Present	65,536	6.06	0.74

includes the proposed methodology, AMROC-LBM with adaptive mesh refinement, AMROC-LBM* with a fixed patch, and AMROC-LBM (uni.) with uniform grids. The CPU time is measured on the University of Southampton cluster, IRIDIS 4. Each simulation was run on 2.6 GHz Intel Sandybridge processors. The standard LBM with uniform grids is known for its rather straightforward implementation, and its efficient computational algorithm. However, it can be quite time-consuming for performing external aerodynamics simulations where there is a need for relatively large domains and high resolution near the body [33]. The most established way to work around this issue is by using blockwise-mesh refinement [34], and as it can be seen in Table 5 the adaptive mesh refinement solutions provide drastically higher levels of accuracy and efficiency than uniform grids. Even further improvements can be made if the present finite-difference scheme is used. The reduction of CPU time is accomplished by the significant reduction of mesh elements, and the improved accuracy by the increased resolution in the desired area by employing the stretching function.

3.4. NACA0012 Aerofoil

Further, the current methodology also has the capacity to solve the flow over slender bodies. NACA profiles have been broadly studied, and there is plenty of literature available which ease the validation. Therefore, the present methodology has been implemented on the NACA0012 aerofoil in the low Reynolds numbers regime to demonstrate its capability to solve the flow over aerofoils. Traditional LBM solvers struggle when solving the flow over slender bodies since there is a boundary layer formation. The use of Cartesian grids can become impractical especially when a boundary layer is thin. Given its inherent difficulty, instead of resolving the flow, standard LBM solvers commonly use turbulence and wall models to achieve an approximate representation of the flow field [35]. The advantage of the body fitted strategy is that the mesh elements in the boundary layer can be staggered in the wall-normal direction and therefore capture the large gradients exhibited.

For the following cases, an O-grid with a domain size of 15 chord lengths is used. The boundary conditions for all the simulations presented are done in the same manner as the 2D circular cylinder previously presented. Figure 11 shows the mesh elements close to the aerofoil surface and also a close-up of the leading edge and the trailing edge. A third-party code, Construct2D, is used to generate this grid because there are no analytic mapping functions for this geometry. Therefore, the metrics are obtained numerically using second-order finite differences. An elliptic grid generator is used to make the grid lines approximately orthogonal to the aerofoil surface, and an appropriate clustering is employed for properly resolving the laminar boundary layer. Flow fields are computed for Re = 500 at 0° and 10° incidence angle, and for a significantly higher Reynolds number, Re = 12000 at 0° and 5° incidence.

Table 6: Minimum aerofoil spacing and resolution for the NACA0012 Re = 500 at 0° angle of attack.

Method	Δy_{min}	Resolution (on surface)
CFL3D	1.2×10^{-4}	52,593
PowerFLOW	7.8×10^{-4}	418,800 (1275)
GILBM	4.5×10^{-4}	52,593 (251)
Present	3.5×10^{-4}	66,049 (257)

The first test case is a relatively low Reynolds number, Re = 500, at 0° angle of attack. For this test case, a grid size of 257 × 257 is used and our results are compared with others [7, 36]. Imamura and Suzuki [7] also have solved the LBM in generalised coordinates for this test case, but using an interpolation strategy (GILBM). Lockard et al. [36] have made a detailed comparison of a commercial Cartesian LBM solver (PowerFLOW) on static multi-resolution meshes with a conventional Navier-Stokes (CFL3D) for the flow over a 2D NACA0012 over a quite vast range of Reynolds numbers, in which our first test

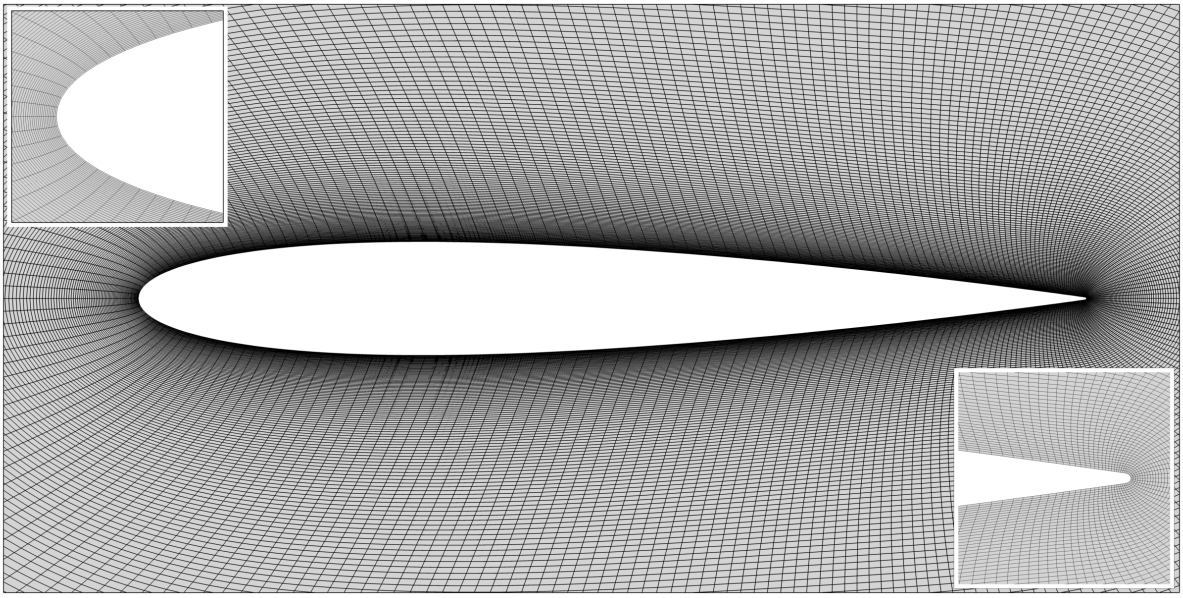

Figure 11: Body-fitted grid used for NACA0012 aerofoil. Overlaid on the upper-left is a close-up of the leading edge and on the lower-right the trailing edge.

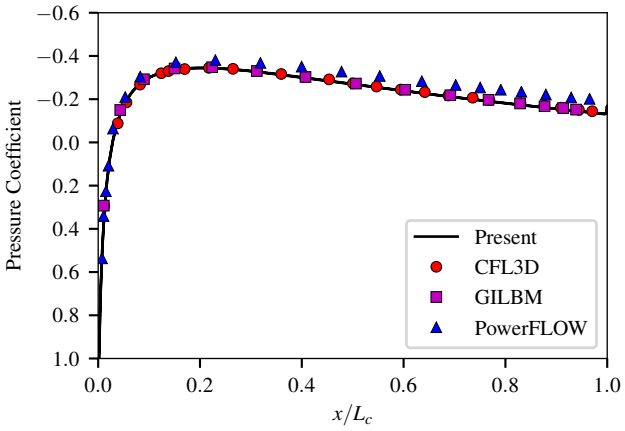

Figure 12: Pressure coefficient distribution for Re = 500 at 0° angle of attack.

case is included. Figure 12 shows the pressure coefficient over the aerofoil surface obtained by the different methods. In this plot, we can see that our results have a better agreement with what is considered the reference solution (CFL3D) than the Cartesian LBM in PowerFLOW. Differences between PowerFLOW and the reference solution increase downstream, as it can be seen in Figure 12. This might suggest that the boundary layer from PowerFLOW is not properly resolved. Note that the meshing and simulation strategy applied in PowerFlow is the same as in the cases denoted AMROC-LBM* in the previous section.

Table 6 compares the resolution of the different methods used to compute the pressure coefficient over the aerofoil surface shown in Figure 12. It can be observed that the Cartesian LBM solver requires a significantly higher number of mesh elements than the non-Cartesian methodologies, and it still has discrepancies compared with the rest of the solvers. This might be due to the lack of wall-normal grid resolution near the surface.

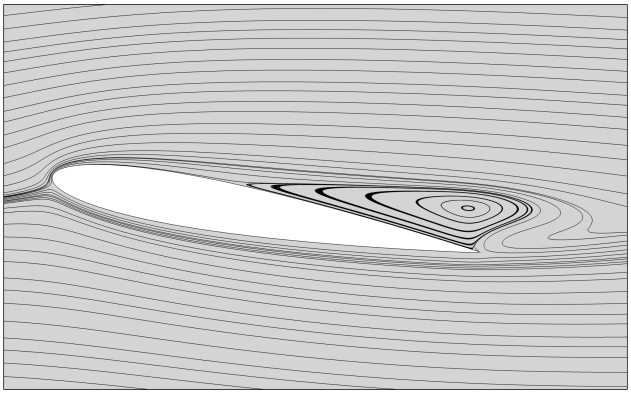

Figure 13: Flow field shown by the streamlines for Re = 500 at 10° angle of attack.

The second test case is done with the same grid and at the same Reynolds number but at 10° angle of attack. At 0° the flow remains fully attached, but at 10° there is a steady recirculation region near the trailing edge. This phenomenon is shown by the streamlines which can be observed on Figure 13. Our solutions are being compared to the results of Hafez et al. [37]. Using a viscous/inviscid interaction procedure coupling potential flow with boundary layer calculations, Hafez et al. provide a very accurate numerical result for laminar flow over the NACA0012 aerofoil. Figure 14 shows that the present method has an

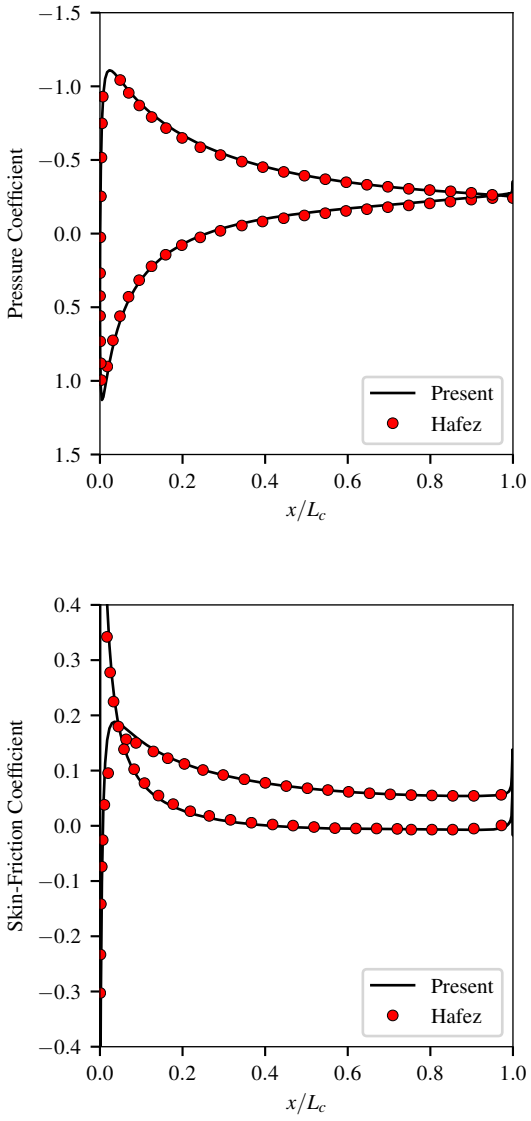

Figure 14: Re = 500 at 10° angle of attack. Top: Pressure coefficient. Bottom: Skin friction coefficient.

excellent agreement with this reference.

The next test cases are performed at a significantly higher Reynolds number, Re = 12000, and with a grid size of 701×701. For the following simulations, the characteristic velocity u_∞ is 0.12. Even though this flow regime is also considered laminar, the boundary layer thickness is significantly smaller when compared to Re = 500, therefore these simulations present a bigger challenge. At these flow conditions, several studies are available, although most of them deal with aerodynamics of heaving and pitching aerofoils. At this Reynolds number, the NACA0012 aerofoil acts somewhat similar to bluff bodies [38], since it displays vortex shedding similarly to the flow around the 2D circular cylinder.

This test case for flow at a higher Reynolds number is validated with the experimental data from Koochesfahani

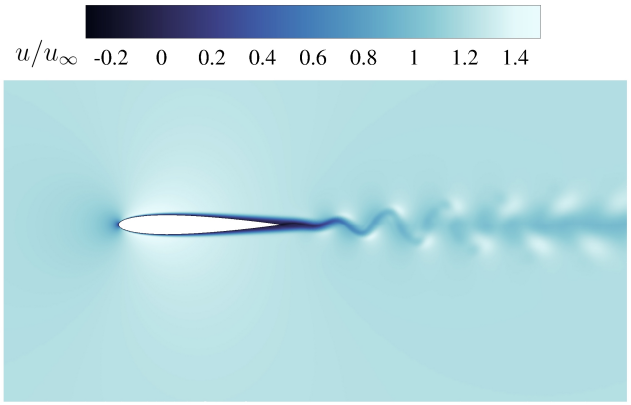

Figure 15: Normalised u-velocity for Re = 12000 at 0° angle of attack.

[39]. The data was obtained by running experiments for the same aerofoil in a low-speed water tunnel at 0° angle of attack. Koochesfahani is reporting a reduced shedding frequency of $k = 8.71$, where

$$k = \frac{\pi f L_c}{u_\infty}, \tag{28}$$

which compares favourably with our value of 8.4. Figure 15 shows the wake being formed by the aerofoil and up to some degree the boundary layer. It can be seen that the wake has an oscillatory solution.

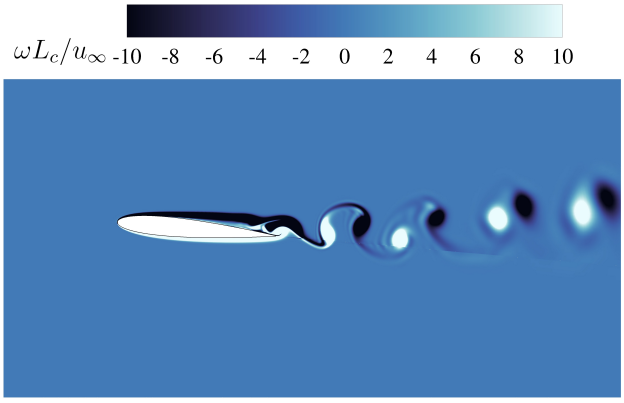

Figure 16: Normalised vorticity for Re = 12000 at 5° angle of attack.

At the same Reynolds number but at 5° angle of attack, a vortex shedding phenomenon also occurs. Figure 16 shows the instantaneous vorticity and Figure 17 shows the unsteady wake formation behind the aerofoil. At these conditions, the flow separates upstream of the trailing edge, and both sides of the aerofoil shed vortices alternatingly in a similar manner to the shedding behind a circular cylinder. A few recirculation regions are formed. These recirculation regions are shown by instantaneous streamlines that are seen in Figure 18.

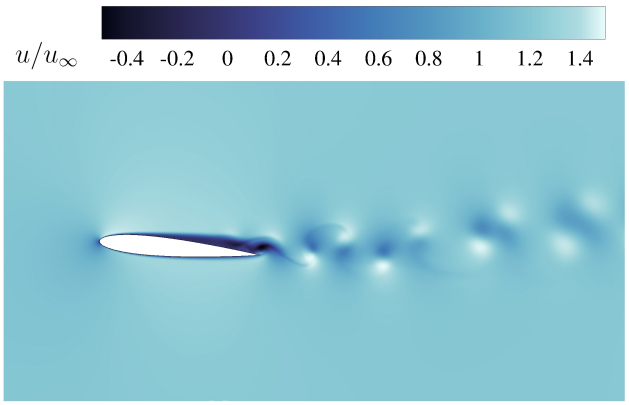

Figure 17: Normalised u-velocity for Re = 12000 at 5° angle of attack.

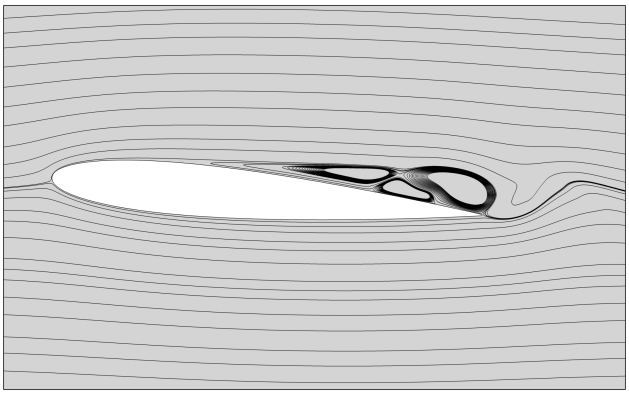

Figure 18: Flow field shown by instantaneous streamlines for Re = 12000 at 5° angle of attack.

4. Conclusions

In this study, it is shown that the second-order scheme used is accurate and suitable for the LBM in generalised curvilinear coordinates, so non-uniform grids can be employed. Numerical results for the decaying Taylor-Green vortex, the 2D lid-driven cavity, the flow around a 2D circular cylinder and the NACA0012 aerofoil are used to analyse the present methodology. The solutions obtained by the present method show good agreement with the available numerical and experimental references. Since the proposed curvilinear treatment alters only the streaming operator of a lattice Boltzmann method, it is straightforward to extend the presented scheme to three space dimensions, and it would equally be possible to consider other collision operators [16], for instance, for stricter incompressibility preservation if desired.

One of the advantages of utilising non-uniform grids is the capacity of using large domains without adding many grid points. Resolution can be increased in areas of interest and coarser elements can be used in less critical areas, such as the far-field. Besides, having bigger elements at the outer-boundaries may help to minimize the effects of the outflow boundary condition. This can be appreciated when the present methodology is compared directly to a standard LBM solver (AMROC) for the 2D cylinder test case. It is noticeable that the Cartesian solver requires a significantly higher number of elements to have a good representation of the flow behaviour in the vicinity of curved-wall boundary, which leads to an increase in computational effort. Using the LBM on curvilinear coordinates allows using body-fitted meshing to resolve the flow over slender bodies and therefore capturing large gradients in the wall-normal direction with high aspect ratio mesh elements. Even though second-order accurate finite differences are used to get the transformation metrics for the NACA0012, the results presented for this test case are of high quality, and the effects of this approximation are imperceptible.

Central schemes are known for having excellent dissipation properties, but they tend to produce numerical oscillations. A simple way to work around this issue is by adding a linear damping term. A fourth-order damping term should not affect the accuracy of a formal second-order scheme. However, the damping coefficient should be chosen wisely, since if this term is significantly large, it can pollute the solution and lead to inaccurate results. Upwind schemes do not need linear damping to stabilise the solution, but they display significant levels of dissipation, which may not be desirable. Furthermore, the results presented indicate that the scheme is second-order accurate even for curved geometries, and it is capable of solving relevant Reynolds number flow problems over aerodynamically shaped smooth bodies.

It can be expected that the parallel efficiency of the presented non-Cartesian LBM and the standard LBM will be very similar. Both schemes use time-explicit update stencils that require nearest neighbour communication only. The current scheme is using a second-order-accurate central difference for convection that is employing a fourth-order-accurate dissipation term for stabilisation. Thereby, the finite-difference stencil radius of our non-Cartesian implementation is two neighbouring cells, in contrast to the standard LBM that uses one. However, in our adaptive framework AMROC, even the standard LBM is implemented with a ghost cell width of two cells minimum, which turned out to be necessary to facilitate the required density distribution exchange at coarse-fine interfaces [26], and hence no parallel performance penalty is expected when the non-Cartesian LBM will be used within AMROC. This implementation is currently under way. Since the non-Cartesian streaming operation is more compute expensive than the standard streaming, and also interpolation and restriction across different levels of resolution need to consider the curvilinear geometry, the overall computational costs per cell will increase slightly; nonetheless, this will be greatly outweighed by the expected improvements in accuracy.

Acknowledgements

The authors gratefully acknowledge the support of CONACYT (Consejo Nacional de Ciencia y Tecnología) and the use of the IRIDIS High Performance Computing Facility, and associated support services at the University of Southampton, in the completion of this work.

References

[1] S. Chen, G. D. Doolen, Lattice Boltzmann method for fluid flows, Annual Review of Fluid Mechanics 30 (1998) 329–364.

[2] R. Deiterding, S. L. Wood, Predictive wind turbine simulation with an adaptive lattice Boltzmann method for moving boundaries, Journal of Physics: Conference Series 753 (2016) 082005.

[3] D. Yu, R. Mei, L. S. Luo, W. Shyy, Viscous flow computations with the method of lattice Boltzmann equation, Progress in Aerospace Sciences 39 (2003) 329–367.

[4] X. He, L. S. Luo, Theory of the lattice Boltzmann method: From the Boltzmann equation to the lattice Boltzmann equation, Physical Review E 56 (1997) 6811–6817.

[5] X. He, L. Luo, M. Dembo, Some progress in lattice Boltzmann method. Part I. Nonuniform mesh grids, Journal of Computational Physics 129 (1996) 357–363.

[6] X. He, G. Doolen, Lattice Boltzmann method on curvilinear coordinates system: Flow around a circular cylinder, Journal of Computational Physics 134 (1997) 306–315.

[7] T. Imamura, K. Suzuki, Flow simulation around an airfoil by lattice Boltzmann method on generalized coordinates, AIAA 43 (2005) 1968–1973.

[8] R. Mei, W. Shyy, On the finite difference-based lattice Boltzmann method in curvilinear coordinates, Journal of Computational Physics 143 (1998) 426–448.

[9] Z. Guo, T. S. Zhao, Explicit finite-difference lattice Boltzmann method for curvilinear coordinates, Physical Review E 67 (2003) 066709.

[10] S. Succi, G. Amati, R. Benzi, Challenges in lattice Boltzmann computing, Journal of Statistical Physics 81 (1995) 5–16.

[11] M. Stiebler, J. Tölke, M. Krafczyk, An upwind discretization scheme for the finite volume lattice Boltzmann method, Computers and Fluids 35 (2006) 814–819.

[12] D. V. Patil, K. N. Lakshmisha, Finite volume TVD formulation of lattice Boltzmann simulation on unstructured mesh, Journal of Computational Physics 228 (2009) 5262–5279.

[13] S. S. Patel, M. Min, K. C. Uga, T. Lee, A spectral-element discontinuous Galerkin lattice Boltzmann method for simulating natural convection heat transfer in a horizontal concentric annulus, Computers and Fluids 95 (2014) 197–209.

[14] K. Hejranfar, M. Hajihassanpour, Chebyshev collocation spectral lattice Boltzmann method in generalized curvilinear coordinates, Computers and Fluids 146 (2017) 154–173.

[15] Y. H. Qian, D. D'Humières, P. Lallemand, Lattice BGK models for Navier-Stokes equation, Europhysics Letters 17 (1992) 479–484.

[16] Z. Guo, C. Shu, Lattice Boltzmann Method and its Applications in Engineering, World Scientific, 2013.

[17] K. A. Hoffmann, S. T. Chiang, Computational Fluid Dynamics -Volume I, Engineering Education System, 2000.

[18] C. Hirsch, Numerical Computation of Internal and External Flows, Wiley, 1988.

[19] Y. Li, Wavenumber-extended high-order upwind-biased finite-difference schemes for convective scalar transport, Journal of Computational Physics 133 (1997) 235–255.

[20] C. K. Tam, Computational aeroacoustics: An overview of computational challenges and applications, International Journal of Computational Fluid Dynamics 18 (2004) 547–567.

[21] T. Kruger, H. Kusumaatmaja, A. Kuzmin, O. Shardt, S. Goncalo, E. M. Viggen, The Lattice Boltzmann Method - Principles and Practice, Springer International Publishing, 2017.

[22] U. Ghia, K. N. Ghia, C. T. Shin, High-resolutions for incompressible flows using Navier-Stokes equations and a multigrid method, Journal of Computational Physcis 48 (1982) 387–411.

[23] S. Hou, Q. Zou, S. Chen, G. Doolen, A. C. Cogley, Simulation of cavity flow by the lattice Boltzmann method, Journal of Computational Physics 118 (1995) 329–347.

[24] R. Deiterding, Block-structured adaptive mesh refinement - theory, implementation and application, ESAIM: Proceedings 34 (2011) 97–150.

[25] H. Chen, O. Filippova, J. Hoch, K. Molvig, R. Shock, C. Teixeira, R. Zhang, Grid refinement in lattice Boltzmann methods based on volumetric formulation, Physica A: Statistical Mechanics and its Applications 362 (2006) 158–167.

[26] R. Deiterding, S. L. Wood, An adaptive lattice Boltzmann method for predicting wake fields behind wind turbines, in: New Results in Numerical and Experimental Fluid Mechanics X, Springer International Publishing, 2016, pp. 845–857.

[27] Z. L. Guo, C. G. Zheng, B. C. Shi, Non-equilibrium extrapolation method for velocity and pressure boundary conditions in the lattice Boltzmann method, Chinese Physics (Overseas Edition) 11 (2002) 366–374.

[28] D. Tritton, Experiments on the flow past a circular cylinder at low Reynolds numbers, Journal of Fluid Mechanics 6 (1959) 547–567.

[29] R. D. Henderson, Details of the drag curve near the onset of vortex shedding, Physics of Fluids 7 (1995) 2102–2104.

[30] S. C. R. Dennis, G. Chang, Numerical solutions for steady flow past a circular cylinder at Reynolds numbers up to 100, Journal of Fluid Mechanics 42 (1970) 471–489.

[31] A. S. Grove, F. H. Shair, E. E. Petersen, A. Acrivos, An experimental investigation of the steady separated flow past a circular cylinder, Journal of Fluid Mechanics 19 (1964) 60–80.

[32] P. H. Chiu, R. K. Lin, T. W. Sheu, A differentially interpolated direct forcing immersed boundary method for predicting incompressible Navier-Stokes equations in time-varying complex geometries, Journal of Computational Physics 229 (2010) 4476–4500.

[33] S. Sen, S. Mittal, G. Biswas, Steady separated flow past a circular cylinder at low Reynolds numbers, Journal of Fluid Mechanics 620 (2009) 89–119.

[34] Y. Dazhi, R. Mei, W. Shyy, A multi-block lattice Boltzmann method for viscous fluid flows, International Journal for Numerical Methods in Fluids 39 (2002) 99–120.

[35] D. M. Holman, R. M. Brionnaud, M. Chávez-Modena, E. Valero-Sánchez, Lattice Boltzmann method contribution to the second high-lift prediction workshop, Journal of Aircraft 52 (2015) 1122–1135.

[36] D. P. Lockard, L. S. Luo, S. D. Milder, B. A. Singer, Evaluation of PowerFLOW for aerodynamic applications, Journal of Statistical Physics 107 (2002) 423–478.

[37] M. Hafez, A. Shatalov, M. Nakajima, Improved numerical simulations of incompressible flows based on viscous/inviscid interaction procedures, Computational Fluid Dynamics 2006 - Proceedings of the Fourth International Conference on Computational Fluid Dynamics, ICCFD 2006 36 (2009) 309–314.

[38] J. Young, J. C. Lai, Vortex lock-in phenomenon in the wake of a plunging airfoil, AIAA Journal 45 (2007) 485–490.

[39] M. M. Koochesfahani, Vortical pattern in the wake of an oscillating airfoil, AIAA Journal 27 (1989) 1200–1205.